Electronic Supplementary Material (ESI) for Chemical Communications.

Supporting Information

Aurophilicity Under Pressure: A Combined Crystallographic and *In-situ* Spectroscopic Study

Alice E. O'Connor,[a] Nedaossadat Mirzadeh,[a,b,*] Suresh K. Bhargava,[b] Timothy L. Easun,[c] Martin Schröder[a,d,*] and Alexander J. Blake[a,*]

[a] School of Chemistry, The University of Nottingham, University Park, Nottingham, NG7 2RD, UK.

[b] Centre for Advanced Materials & Industrial Chemistry, School of Applied Sciences, RMIT University, GPO Box 2476V, Melbourne, Victoria 3001, Australia.

[c] School of Chemistry, Main Building, Cardiff University, Park Place, Cardiff, CF10 3AT, UK.

[d] School of Chemistry, Oxford Road, University of Manchester, Manchester, M13 9PL, UK.

Contact author email: a.j.blake@nottingham.ac.uk

Contents

1. Synthesis of 1,4-[$C_6H_4\{PPh_2(AuCl)\}_2$] (1)

All commercially available reagents were used as received without further purification and [1,4-$C_6H_4\{PPh_2(AuCl)\}_2$] **(1)** was synthesised according to a literature procedure.[1] The resulting white solid was recrystallized by vapour diffusion of pentanes into a solution of the complex in dichloromethane to yield colourless, block-shaped crystals.

2. High pressure crystallographic studies

High pressure experiments were carried out using a Merrill-Basset diamond anvil cell (DAC) [opening angle 37° (2θ), culet faces 600 μm, WC backing plates and 100 × 100 × 0.02 mm tungsten gaskets, gasket hole diameter of 200 μm]. A colourless crystal of **1** (0.075 × 0.05 × 0.01 mm) was loaded into the DAC, along with a ruby sphere as the pressure calibrant and 4:1 methanol/ethanol as the pressure-transmitting medium (PTM). Diffraction data were collected using Mo-K_α radiation (λ = 0.71073 Å, microfocus source, focussing mirrors) on an in-house Agilent SuperMova diffractometer equipped with an Eos CCD detector. Diffraction data were processed using the program *CrysAlisPRO*[2] and absorption corrections were applied using SADABS.[3] Diffraction data were collected at ambient pressure and at 5.3, 10.2, 30.2, 39.1, 51.8, 69.5, 74.2, 93.9, 97.9, 102.2 and 106.2 kbar. Pressure measurements were carried out using the ruby fluorescence method.[4] Prior to the loading of the PTM, framesets were collected on a crystal inside the DAC at ambient pressure and temperature to provide a good starting model for structure refinement. Lattice parameters for **1** could be extracted for all pressures studied. Structures were solved by transferring the fractional coordinates of the atoms as determined at an adjacent pressure and refined using SHELXL,[5] satisfactory structural refinements were obtained from all datasets, including anisotropic treatment of all non-hydrogen atoms. Due to the inherent low completeness of the diffraction data caused by the presence of the diamond anvil cell, restraints were required. The following restraints were employed for all structures: similarity restraints (0.02 Å) were applied to the C-C bonds of the phenyl rings. As is normal in high pressure experiments, the data quality does deteriorate at higher pressures, so some additional restraints had to be applied to these structures in the form of explicit distance restraints [1.39(2) Å] to the C-C bonds of the phenyl rings. Where necessary, rigid-body restraints [0.004 Å^2] were applied to the whole structure.

Upon further analysis of the data, it was clear that there was a lack of data points in the range 10-30 kbar, so a second crystal of **1** (0.045 × 0.027 × 0.018 mm) was loaded into a DAC and diffraction data were collected at 19.6 kbar. Data processing and structural refinement was carried out as described above.

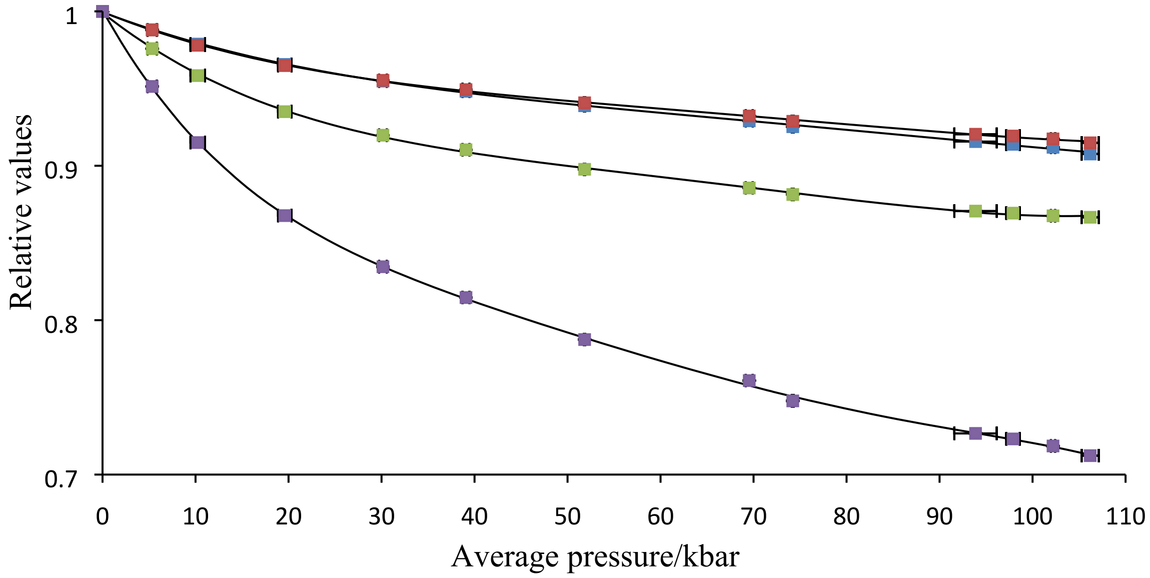

Figure S1. Variation in the relative unit cell parameters and volume with increasing pressure: a/a_0 – blue squares, b/b_0 – red squares, c/c_0 – green squares, V/V_0 – purple squares. The horizontal error bars relate to the range in pressure over the data collection; the pressure is recorded before and after the data collection and an average value is calculated. Where not visible, the error bars are smaller than the symbols.

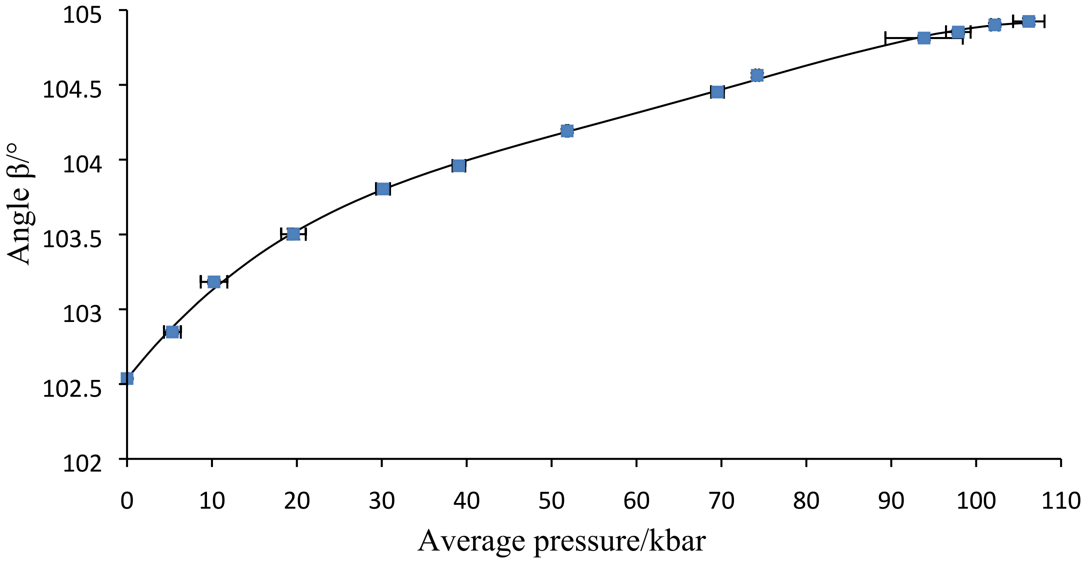

Figure S2. Variation in the absolute value of the β angle with increasing pressure. The horizontal error bars relate to the range in pressure over the data collection; the pressure is recorded before and after the data collection and an average value is calculated. Where not visible, the error bars are smaller than the symbols.

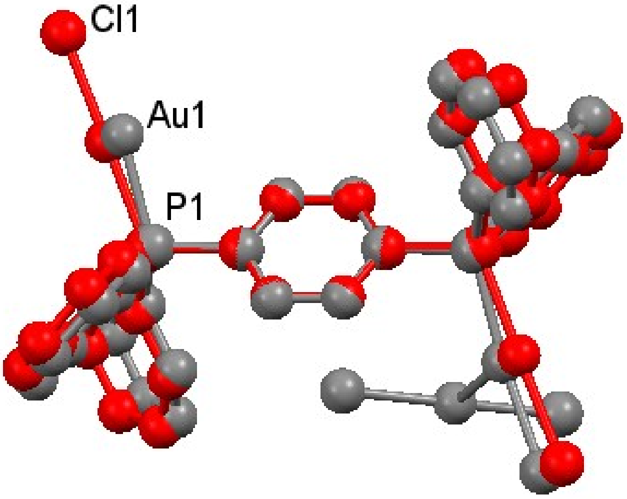

Figure S3. A least-squares fit (RMSD = 0.0216 Å) of the structures of **1** at ambient pressure (red) and 106.2 kbar (grey).

Table S1. Crystallographic data for **1** between ambient pressure and 106.2 kbar.

Pressure (kbar)	**0.001**	**5.3**	**10.2**	**19.6**	**30.1**	**39.1**	**51.8**	**69.5**	**74.2**	**93.9**	**97.9**	**102.2**	**106.2**
***a*, *b*, *c* (Å)**	17.4201 (3), 13.47890 (19), 12.0817 (2)	17.2129 (5), 13.3158 (5), 11.7900 (5)	17.0509 (5), 13.1824 (5), 11.5790 (5)	16.8213 (16), 13.0052 (17), 11.2967 (18)	16.6333 (6), 12.8767 (6), 11.1124 (7)	16.5181 (4), 12.7957 (5), 10.9986 (5)	16.3552 (4), 12.6807 (5), 10.8457 (5)	16.1848 (4), 12.5654 (5), 10.6996 (5)	16.1185 (6), 12.5191 (7), 10.6485 (6)	15.9507 (6), 12.4062 (7), 10.5188 (7)	15.9198 (6), 12.3906 (7), 10.5027 (7)	15.8861 (4), 12.3656 (5), 10.4819 (5)	15.8107 (7), 12.3314 (8), 10.4704 (8)
β (°)	102.5369 (17)	102.848 (4)	103.183 (4)	103.502 (12)	103.804 (5)	103.959 (4)	104.192 (4)	104.452 (4)	104.564 (5)	104.813 (5)	104.853 (5)	104.901 (4)	104.924 (7)
***V* (Å^3)**	2769.37 (8)	2634.65 (17)	2534.04 (17)	2403.0 (6)	2311.3 (2)	2256.03 (15)	2180.70 (15)	2107.11 (14)	2079.71 (19)	2012.4 (2)	2002.5 (2)	1989.83 (14)	1972.5 (2)
μ (mm^{-1})	10.91	11.47	11.92	12.57	13.07	13.39	13.86	14.34	14.53	15.01	15.09	15.18	15.32
T_{min}, T_{max}	0.385, 0.583	0.372, 0.431	0.372, 0.431	0.653, 0.746	0.384, 0.431	0.368, 0.431	0.388, 0.431	0.395, 0.431	0.378, 0.431	0.369, 0.431	0.375, 0.431	0.393, 0.431	0.380, 0.431
No. of measured, independent and observed [$I > 2\sigma(I)$] reflections	8824, 3078, 2641	10849, 1374, 1120	9794, 1266, 1068	9341, 1195, 735	9473, 1220, 1073	8880, 1159, 1007	8477, 1085, 966	8412, 1081, 975	8884, 1124, 1019	8412, 1081, 963	8481, 1075, 961	8081, 1021, 901	8126, 1027, 887
R_{int}	0.022	0.053	0.051	0.172	0.044	0.053	0.042	0.041	0.042	0.042	0.043	0.041	0.040
$R[F^2 > 2\sigma(F^2)]$, $wR(F^2)$, S	0.024, 0.050, 1.03	0.029, 0.055, 1.08	0.026, 0.051, 1.10	0.059, 0.096, 1.08	0.023, 0.050, 1.09	0.027, 0.064, 1.10	0.023, 0.053, 1.09	0.026, 0.061, 1.08	0.023, 0.054, 1.06	0.021, 0.052, 1.07	0.022, 0.051, 1.08	0.023, 0.052, 1.05	0.027, 0.061, 1.13
No. of reflections	3078	1374	1266	1195	1220	1159	1085	1081	1124	1081	1075	1021	1027
No. of parameters	163	163	163	158	163	163	163	163	163	163	163	163	163
No. of restraints	0	168	168	148	38	171	181	182	182	185	185	158	170

For all structures: M_r = 911.26, monoclinic, $C2/c$, $Z = 4$ and chemical formula = $C_{30}H_{24}Au_2Cl_2P_2$. Experiments were carried out at 293 K with Mo *K*α radiation (λ = 0.71073 Å) using an Agilent SuperNova diffractometer with a single microfocus source at offset and an Eos CCD detector. H-atom parameters were constrained to ride on their parent atoms.

Table S2. Variations in selected bond lengths and bond angles with increasing pressure from ambient pressure to 106.2 kbar.

Bond distance (Å)	**0.001**	**5.3**	**10.2**	**19.6**	**30.2**	**39.1**	**51.8**	**69.5**	**74.2**	**93.9**	**97.9**	**102.2**	**106.2**
Au1-P1	2.2256(16)	2.225(2)	2.2245(18)	2.225(5)	2.2186(16)	2.216(2)	2.2148(17)	2.211(2)	2.2099(17)	2.2053(17)	2.2044(19)	2.2047(18)	2.202(3)
Au1-Cl1	2.2725(17)	2.273(2)	2.2724(19)	2.278(5)	2.2691(17)	2.269(2)	2.2661(17)	2.262(2)	2.2590(17)	2.2521(16)	2.2524(18)	2.2524(18)	2.250(2)
P1-C1	1.814 (7)	1.808(9)	1.796(8)	1.794(19)	1.800(8)	1.807(10)	1.796(8)	1.798(10)	1.802(8)	1.780(7)	1.786(8)	1.785(8)	1.790(12)
P1-C7	1.815 (8)	1.820(9)	1.814(8)	1.79(2)	1.800(8)	1.795(10)	1.794(8)	1.786(10)	1.781(8)	1.756(7)	1.767(8)	1.761(8)	1.739(11)
P1-C13	1.819 (7)	1.810(8)	1.810(7)	1.806(19)	1.790(7)	1.776(9)	1.773(7)	1.778(8)	1.764(7)	1.753(7)	1.738(7)	1.757(7)	1.757(10)
Au1-Au1	3.6686(5)	3.6306(8)	3.5905(8)	3.512(19)	3.4385(8)	3.3870(9)	3.3067(7)	3.2181(9)	3.1857(7)	3.1042(7)	3.0920(8)	3.0761(8)	3.0554(11)
Bond angle (°)	**0.001**	**5.3**	**10.2**	**19.6**	**30.2**	**39.1**	**51.8**	**69.5**	**74.2**	**93.9**	**97.9**	**102.2**	**106.2**
P1-Au1-Cl1	179.11(8)	179.26(10)	179.15(8)	178.6(2)	178.48(8)	177.92(11)	176.93(9)	175.55(11)	175.11(9)	173.78(8)	173.46(9)	173.20(9)	172.62(13)
C1-P1-Au1	115.7(2)	117.1(3)	117.6(2)	119.5(6)	119.5(2)	120.0(3)	120.8(2)	121.8(3)	122.1(2)	122.9(2)	123.1(2)	123.2(2)	122.9(3)
C1-P1-C7	105.4(3)	105.1(4)	105.3(3)	104.3(8)	104.5(3)	104.4(4)	104.4(3)	104.1(4)	104.2(3)	103.8(3)	104.0(3)	104.0(3)	104.1(5)
C1-P1-C13	104.4(3)	104.0(4)	104.2(3)	103.3(8)	103.3(3)	103.2(4)	102.7(3)	102.5(4)	102.0(3)	102.3(3)	101.8(3)	101.6(3)	102.3(5)
C7-P1-Au1	113.0(2)	112.9(2)	112.9(2)	113.4(5)	113.5(2)	113.5(3)	113.8(2)	114.5(3)	114.5(2)	114.6(2)	114.8(2)	114.6(2)	114.7(3)
C7-P1-C13	105.4(3)	105.7(4)	105.3(3)	106.3(8)	105.3(3)	105.4(4)	105.1(3)	104.4(4)	104.4(3)	104.4(3)	104.6(3)	104.4(3)	104.4(4)
C13-P1-Au1	112.1(2)	111.0(2)	110.5(2)	108.9(6)	109.5(2)	109.0(3)	108.5(2)	107.6(3)	107.7(2)	106.9(2)	106.5(2)	106.8(2)	106.4(3)

3. Equation of state calculations

Equation of state calculations were carried out using EOSFit7c[6] whereby the application of different orders of the Birch-Munaghan equation of state revealed that the third-order plot exhibited the best fit to the data and predicted a unit cell volume that was in good agreement with the experimental value (Table S3). It also gave a bulk modulus value which is in good agreement with other Au(I) complexes that have been studied at elevated pressures.

Table S3. Fitting of Birch-Murnaghan equations of state to the unit cell volume.

	Parameter			
Equation of state fitted (Birch-Murnaghan)	V_0/Å^3	K_0/GPa	K'	K''
Second order	2665(10)	14.2(4)	4.00 (implied value)	-0.27475 (implied value)
Third order	2769(16)[a]	8(1)	8(2)	-3.87181 (implied value)
Fourth order	2769(10)	13(10)	2(8)	1(1)

[a] At ambient pressure the experimental value for the unit cell volume is 2769.37(8) Å^3.

4. Analysis of intermolecular interactions

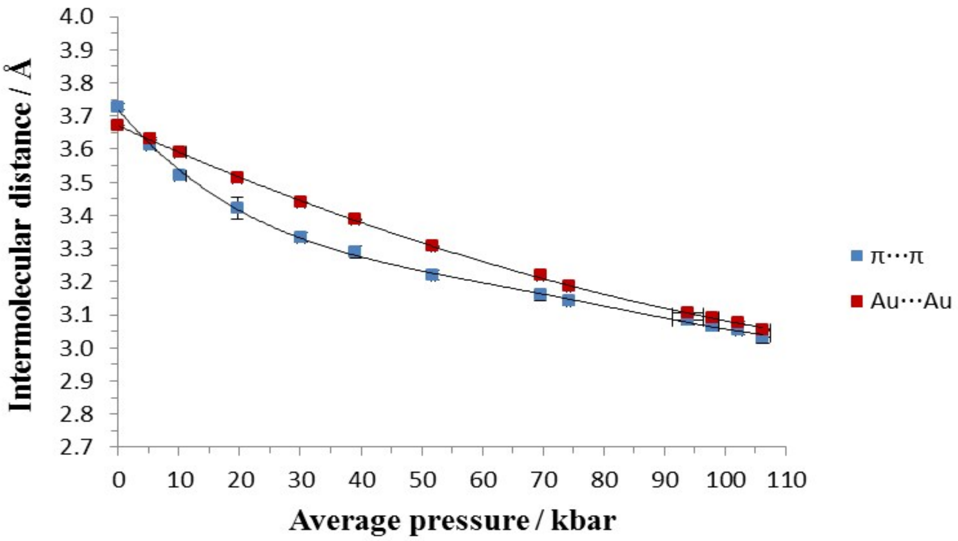

Figure S4. Variation of the Au···Au and centroid-centroid distance in **1** with increasing pressure. Where they are not visible, error bars are smaller than the corresponding symbols.

4.1 Analysis of Au···Au interactions

Analysis of the Au···Au distances across the pressure range studied precludes the possibility of any significant metallic character: excluding the short Au···Au distance we have identified, there are no close Au···Au contacts below *ca.* 8 Å at ambient pressure or below *ca*. 6.5 Å at 106.2 kbar.

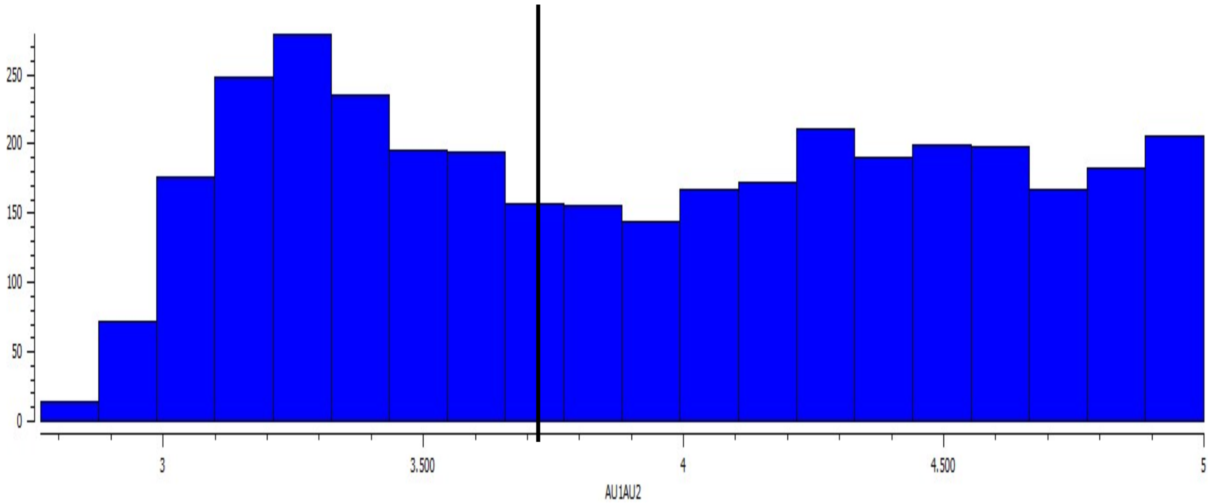

Figure S5. CSD database entries showing the frequency of intermolecular Au···Au interactions as a function of their length at ambient pressure. The black vertical line denotes the position of the Au···Au interaction in **1**.

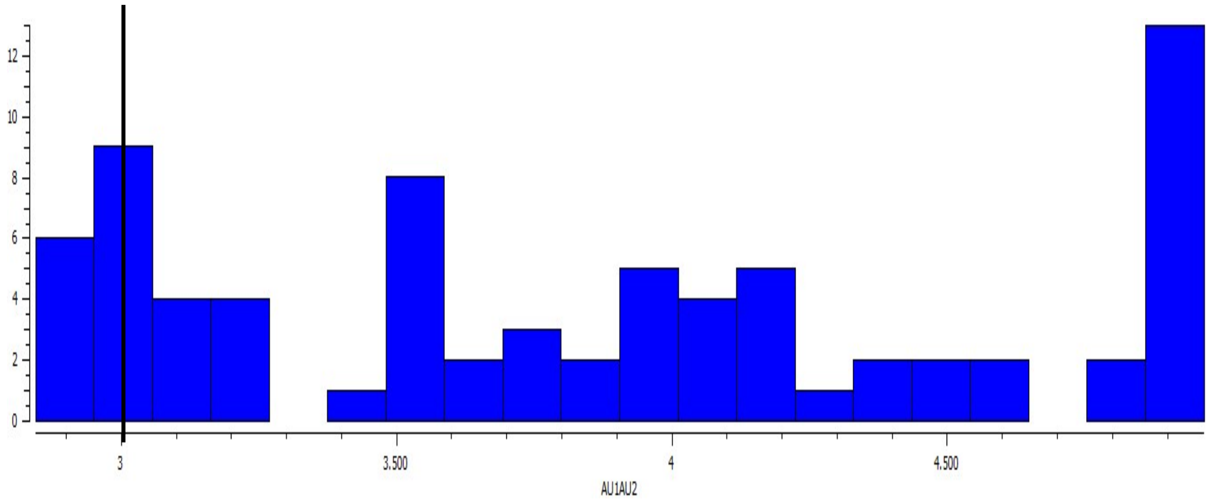

Figure S6. CSD database entries showing the frequency of intermolecular Au···Au interactions as a function of their length under pressure. The black vertical line denotes the position of the Au···Au interaction in **1** the lower end of the length range.

4.2 Analysis of π···π interactions

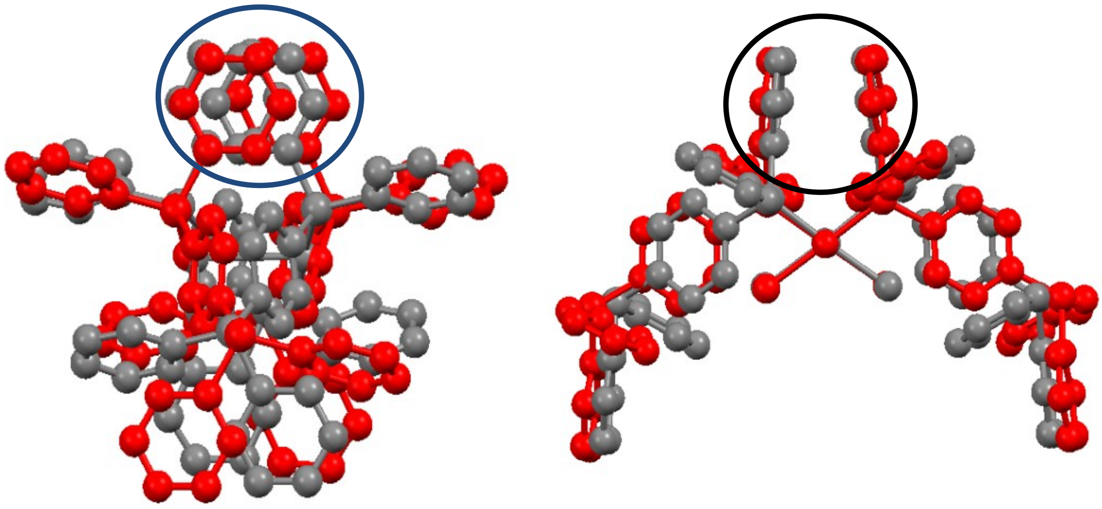

a) b)

Figure S7. View of π···π interactions of **1**, showing the face-to-face interactions present; a) variation in ring overlap with increasing pressure highlighted by blue circle, b) variation in centroid-centroid distance with increasing pressure highlighted by black circle. red – ambient pressure, grey – 106.2 kbar. H atoms are omitted for clarity.

Table S4. Distance parameters related to the π···π interactions in **1**.

Pressure /kbar	**π···π interaction (plane centroid-plane centroid distance/Å**	**Perpendicular distance/Å**	**α/°[a]**
0.001	3.728(3)	-	177.4(2)
5.3	3.613(5)	3.376(4)	177.4(2)
10.2	3.520(4)	3.278(3)	177.4(2)
19.6	3.423(11)	3.163(7)	177.2(9)
30.2	3.333(4)	3.081(3)	176.7(3)
39.1	3.290(6)	3.039(4)	177.1(4)
51.8	3.220(5)	2.971(3)	176.7(4)
69.5	3.158(6)	2.920(4)	175.7(4)
74.2	3.143(5)	2.906(3)	175.8(4)
93.9	3.082(5)	2.846(3)	175.9(4)
97.9	3.064(5)	2.837(3)	175.6(4)
102.2	3.053(5)	2.824(3)	175.8(4)
106.2	3.031(6)	2.820(4)	175.6(5)

[a] α is the pseudoangle P1–C7···C10 as defined by Wong *et al.*[7]

4.3 Analysis of other intermolecular interactions

Whilst the Au···Au and π···π interactions in **1** are the most obvious intermolecular interactions which change as a function of pressure, several other intermolecular interactions, including of the types C−H···π, π···C−H and H···H, are also noteworthy. The different contacts within the van der Waals limit increase in number from three at ambient pressure to 108 at 106.2 kbar (Table S5). These interactions comprise only C−H···π and π···π interactions at ambient pressure, but at 106.2 kbar the following interactions are present: C−H···π, π···π, H···H, C−H···Cl, Au···Cl, Au···π, Au···H−C, Cl··· π, Au···Au, Au···Cl, P··· π and P··· H−C.

Table S5. Summary of the different types of contacts present as a function of pressure.

Pressure/kbar	**Number of different contacts present < sum of vdW radii**	**Different types of contacts present**
0	3	C−H···π and π···π
5.3	5	C−H···π and π···π.
10.2	10	C−H···π, π···π, H···H, C−H···Cl, Cl··· π.
19.6	25	C−H···π, π···π, H···H, C−H···Cl, Cl··· π, Au···Cl, Au···H−C.
30.2	33	C−H···π, π···π, H···H, C−H···Cl, Cl··· π, Au···Cl, Au···H−C.
39.1	41	C−H···π, π···π, H···H, C−H···Cl, Au···Cl, Au···π, Au···H−C, Cl··· π.
51.8	49	C−H···π, π···π, H···H, C−H···Cl, Au···Cl, Au···π, Au···H−C, Cl··· π, Au···Au.
69.5	79	C−H···π, π···π, H···H, C−H···Cl, Au···Cl, Au···π, Au···H−C, Cl··· π, Au···Au, Au···Cl, P··· π, P··· H−C.
74.2	85	C−H···π, π···π, H···H, C−H···Cl, Au···Cl, Au···π, Au···H−C, Cl··· π, Au···Au, Au···Cl, P··· π, P··· H−C.
93.9	98	C−H···π, π···π, H···H, C−H···Cl, Au···Cl, Au···π, Au···H−C, Cl··· π, Au···Au, Au···Cl, P··· π, P··· H−C.
97.9	100	C−H···π, π···π, H···H, C−H···Cl,

		Au···Cl, Au···π, Au···H–C, Cl··· π, Au ···Au, Au···Cl, P··· π, P··· H–C.
102.2	103	C–H···π, π···π, H···H, C–H···Cl, Au···Cl, Au···π, Au···H–C, Cl··· π, Au ···Au, Au···Cl, P··· π, P··· H–C.
106.2	108	C–H···π, π···π, H···H, C–H···Cl, Au···Cl, Au···π, Au···H–C, Cl··· π, Au ···Au, Au···Cl, P··· π, P··· H–C.

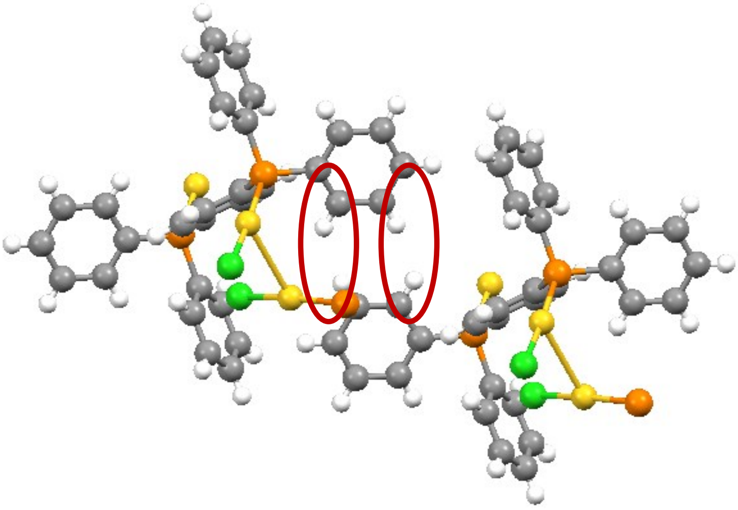

Figure S8. H···H interactions in the same plane at 106.2 kbar.

5. Hirshfeld surface analysis

Hirshfeld surface analysis is a proven and effective tool for visualizing and mapping intermolecular contacts and has allowed us to deepen our understanding of the behaviour of these intermolecular interactions **1** under pressure. The surfaces are generated by partitioning the space in the crystal into regions where the electron distribution of a sum of spherical atoms for the molecule (the pro-molecule) dominates the corresponding sum over the crystal (the pro-crystal). Analysis of the surfaces and contacts for **1** reveals the presence of several types of intermolecular interaction; the number of different contacts increases with pressure (Table S5).

At ambient pressure and 106.2 kbar, specific fingerprint plots were calculated for **1** corresponding to different intermolecular interactions (Figures S8-S12). In all cases, the fingerprint plots show that all of the different types of interactions present become shorter as a function of pressure. The percentage contribution for each type of interaction increases from ambient pressure to 106.2 kbar, except for the contribution for the H···H interactions which decreases (Table S6). Further evidence to support the shortening of all of the intermolecular interactions can be found when analysing the fingerprint plots, which are two-dimensional representations of the distance from the Hirshfeld surface to the nearest nucleus inside the surface (d_i) and outside the surface (d_e).

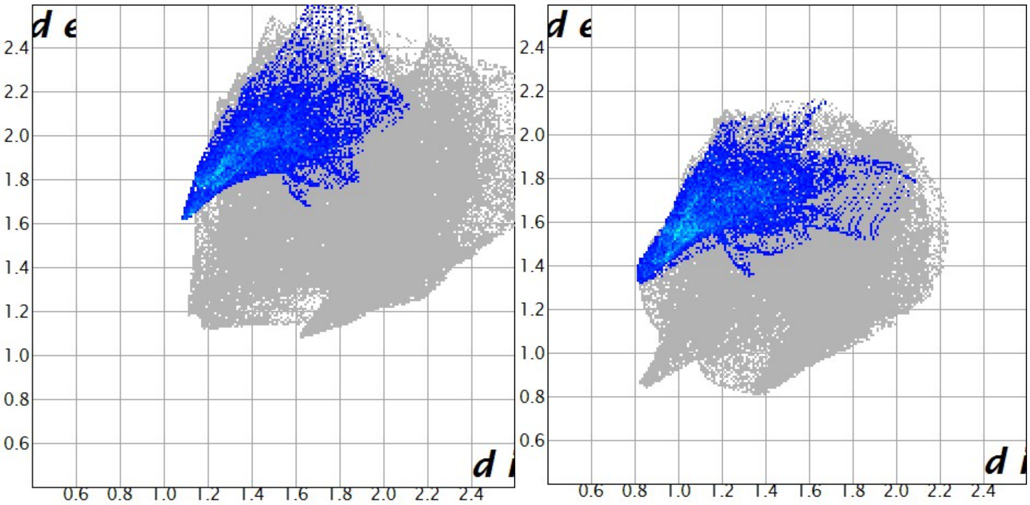

a) b)

Figure S9. Fingerprint plots of a molecule of **1** at a) ambient pressure and b) 106.2 kbar showing the variation in the C−H···π interactions as a function of pressure.

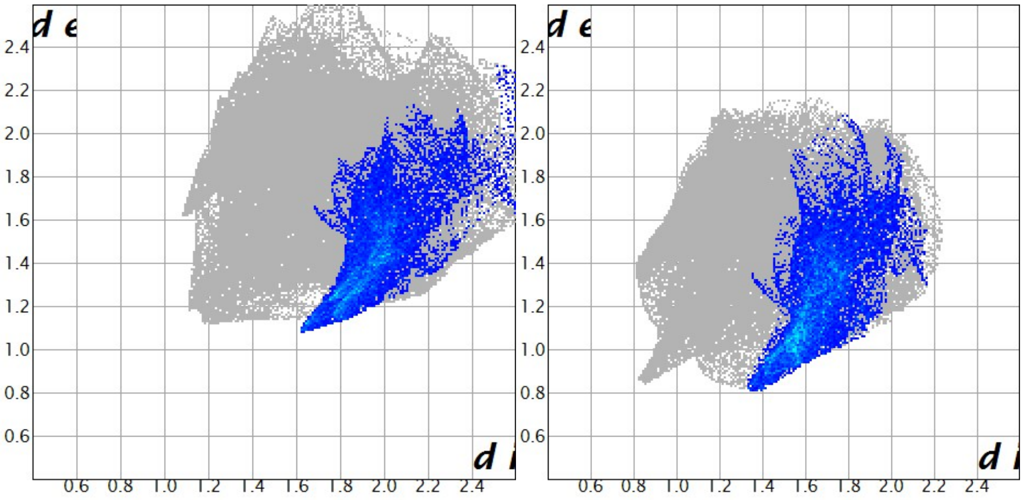

a) b)

Figure S10. Fingerprint plots of a molecule of **1** at a) ambient pressure and b) 106.2 kbar showing the variation in the π···H–C interactions as a function of pressure.

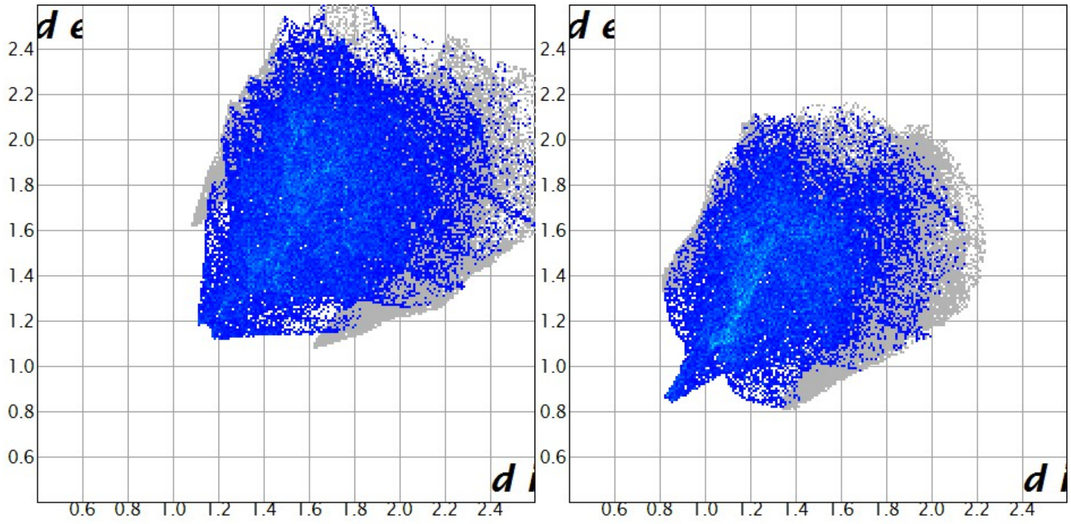

a)

b)

Figure S11. Fingerprint plots of a molecule of **1** at a) ambient pressure and b) 106.2 kbar showing the variation in the H···H interactions as a function of pressure.

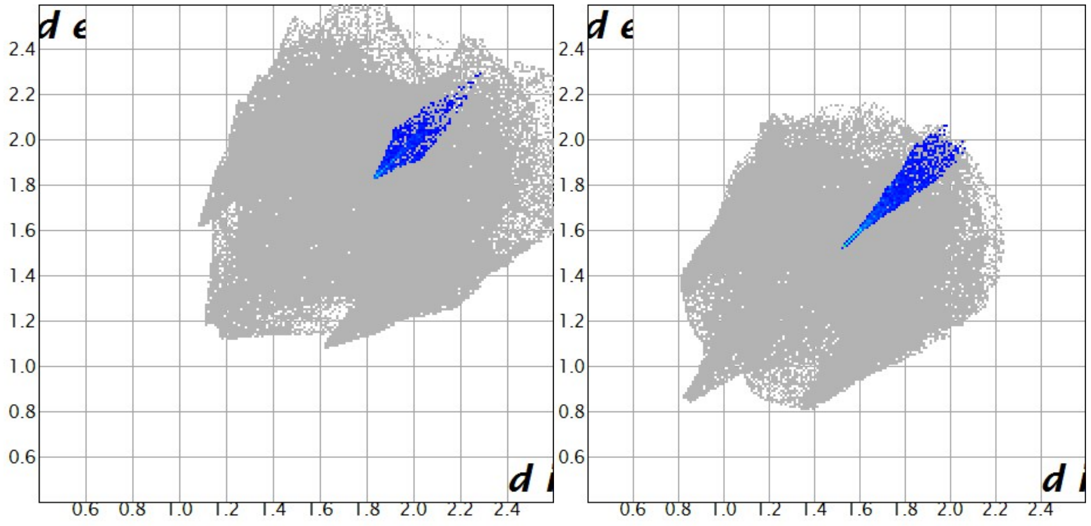

a)

b)

Figure S12. Fingerprint plots of a molecule of **1** at a) ambient pressure and b) 106.2 kbar showing the variation in the Au···Au interactions as a function of pressure.

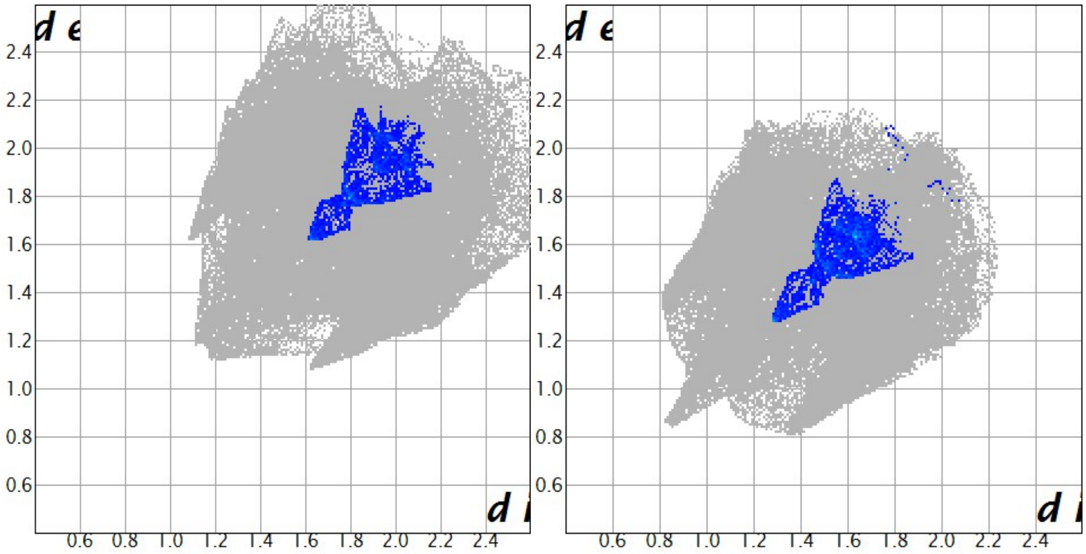

a) b)

Figure S13. Fingerprint plots of a molecule of **1** at a) ambient pressure and b) 106.2 kbar showing the variation in the π···π interactions as a function of pressure.

Table S6. Summary table of the different percentage contributions for the different interactions in the fingerprint plots.

	Percentage contribution of different interactions in the fingerprint plots	
Type of interaction	**Ambient pressure**	**106.2 kbar**
C–H···π	11.4	13.8
π···H–C	12.6	16.4
H···H	41.5	34.6
Au···Au	1	1.6
π···π	2.7	3.4

6. Theoretical calculations

The repulsion energies between two molecules of **1** in geometries defined by the X-ray crystal structures at each pressure were calculated using the ADF2014 suite in the gas phase.[8] Single point energy calculations employed Slater type orbital (STO) triple-ζ-plus polarisation all-electron basis sets (from the ZORA/TZP database of the ADF suite) and used the Perdew-Burke-Ernzerhof (PBE) exchange correlation functional.[9] Scalar relativistic approaches were used within the ZORA Hamiltonian for the inclusion of relativistic effects.

The interactions between two molecules of **1** were examined using an energy decomposition analysis (EDA) that is incorporated into the ADF2014 code. In using this approach, the bonding energy ΔE_{bond} between two molecular fragments is separated into ΔE_{steric} and ΔE_{oi}, where ΔE_{steric} is the steric interaction energy between the two molecular fragments in geometries that are identical to those in the parent molecular grouping and ΔE_{oi} is the orbital contribution to the bonding energy. ΔE_{steric} comprises the destabilising repulsive interactions between occupied molecular orbitals (ΔE_{Pauli}) and the classical electrostatic interaction (ΔE_{elstat}) between the fragments, while ΔE_{oi} accounts for electron pair bonding, charge transfer, and orbital polarisation. The EDA results obtained are listed in Table S7 and shown graphically in Figure S14. At ambient pressure $\Delta E_{bond} = -22.91$ kJ mol^{-1}, indicative of an attractive interaction. Beyond 19.6 kbar, ΔE_{bond} becomes positive and increases to 86.0 kJ mol^{-1} at 106.2 kbar (Table S7), confirming that repulsive energies contribute more to ΔE_{bond}: this result is consistent with the increasing difficulty of compressing the van der Waals space at higher pressures. While ΔE_{oi} becomes more negative, suggesting that orbital overlap becomes more efficient at higher pressure, and the attractive ΔE_{elstat} contributions to ΔE_{steric} energy also become more negative with increasing pressure, it appears these interactions are outweighed by an overall positive ΔE_{Pauli}. Thus, there does not appear to be an overall bonding interaction that drives a compression in bond lengths.

Table S7. Energy decomposition analysis results for **1** as a function of pressure.

Pressure/ kbar	**Pauli repulsion energy/ kJ mol^{-1}**	**Total electrostatic interaction energy/kJ mol^{-1}**	**Total steric interaction energy/kJ mol^{-1}**	**Total orbital energy/ kJ mol^{-1}**	**Total bonding energy/ kJ mol^{-1}**
0	66.19	-55.96	10.23	-33.15	-22.91
5.3	87.37	-65.89	21.48	-38.16	-16.68
10.2	110.8	-77.72	33.09	-43.63	-10.54
19.6	149.85	-99.31	50.54	-52.65	-2.11
30.1	192.61	-121.37	71.24	-61.7	9.54
39.1	221.74	-137.64	84.1	-67.9	16.20
51.8	273.98	-165.48	108.5	-78.86	29.63
69.5	336.45	-198.95	137.5	-91.82	45.68
74.2	356.61	-210.26	146.34	-95.94	50.41
93.9	435.88	-252.85	183.03	-112.35	70.69
102.2	467.61	-268.08	199.53	-118.64	80.90
106.2	489.16	-279.68	209.48	-123.49	86.0

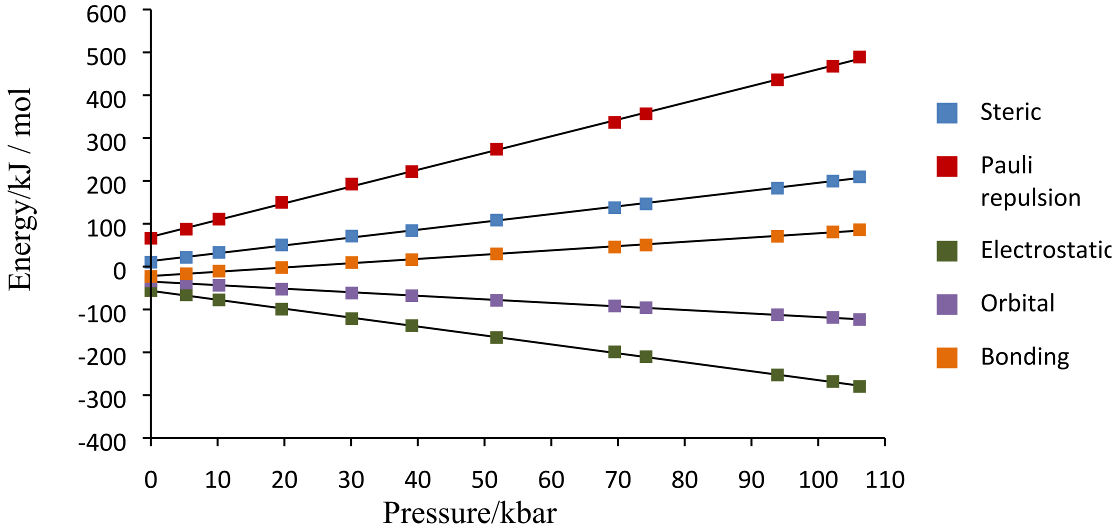

Figure S14. Energy decomposition analysis results for **1** as a function of pressure.

7. Raman spectroscopy

Attempts were made to conduct luminescence experiments on **1** *in-situ* at high pressure but this was not possible due to the presence of the diamond anvil cell and an inability to focus the crystal, so Raman experiments were carried out. Raman experiments were carried out on a Horiba LabRAM HR spectrometer, equipped with laser sources having four different wavelengths to enable coverage of the ultraviolet, visible and near-infrared regions. A crystal of **1** was loaded into the DAC along with 4:1 methanol/ethanol as the hydrostatic fluid. Pressure measurements were recorded using Kawamura's method[10] whereby irradiation of diamond anvils produces a peak in the Raman spectrum at approximately 1330 cm^{-1} due to a C-C stretching mode; the frequency edge of this peak is pressure-dependent and shifts to a higher wavenumber with increasing pressure. The maximum of the diamond peak gives the Raman frequency shift which is used in the pressure calculations (Figure S6 and S7). Raman spectra of **1** were recorded at ambient pressure and at 28.5, 34.3, 58.9 and 81.2 kbar using a 785 nm laser as an excitation source (Figure S8).

$$\mathrm{P(GPa)} \cong A\,\frac{\Delta\omega}{\omega_0}\left[1 + \frac{1}{2}(B-1)\right]\frac{\Delta\omega}{\omega_0}$$

Figure S15. The equation for calculating the pressure inside the DAC. A and B are fitting parameters, ω_0 = 1334 cm^{-1} at ambient pressure, $\Delta\omega$ = frequency shift.

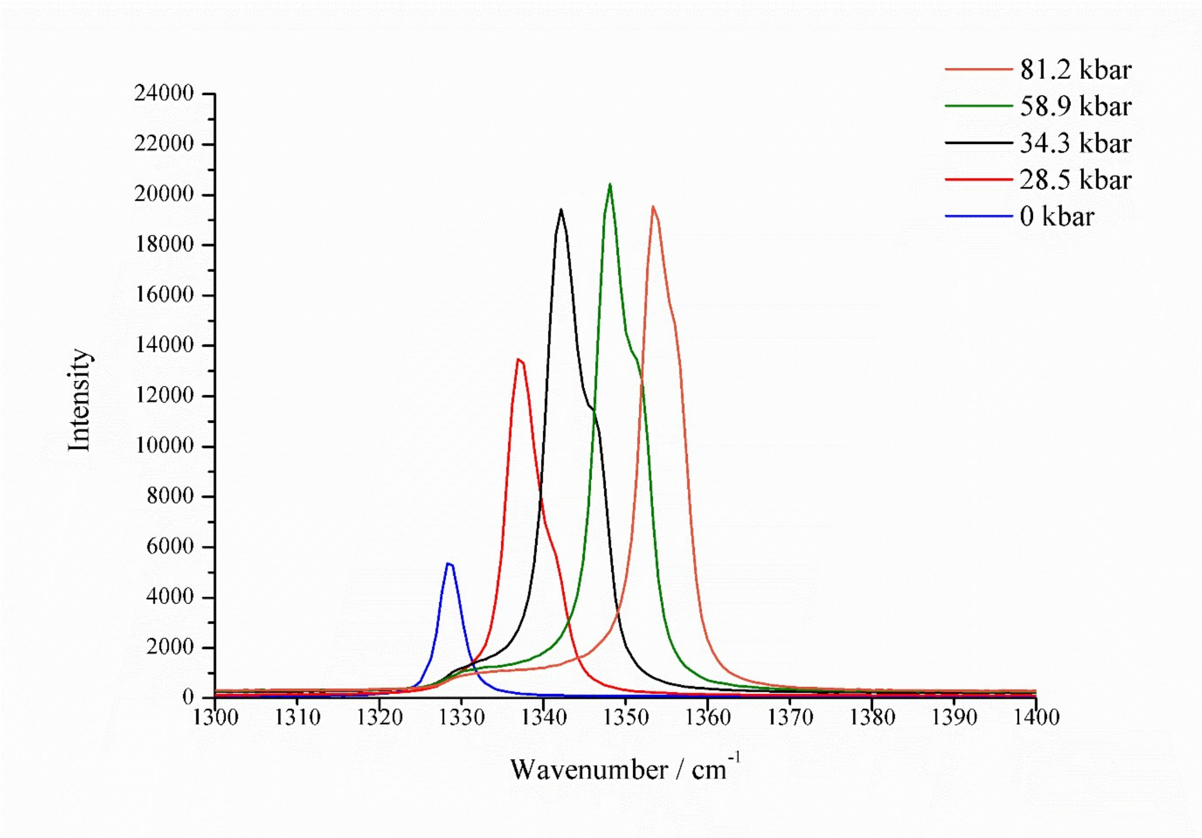

Figure S16. Raman peaks produced by excitation of the diamond anvils using a 785 nm laser. The peak shifts were used to calculate pressures.

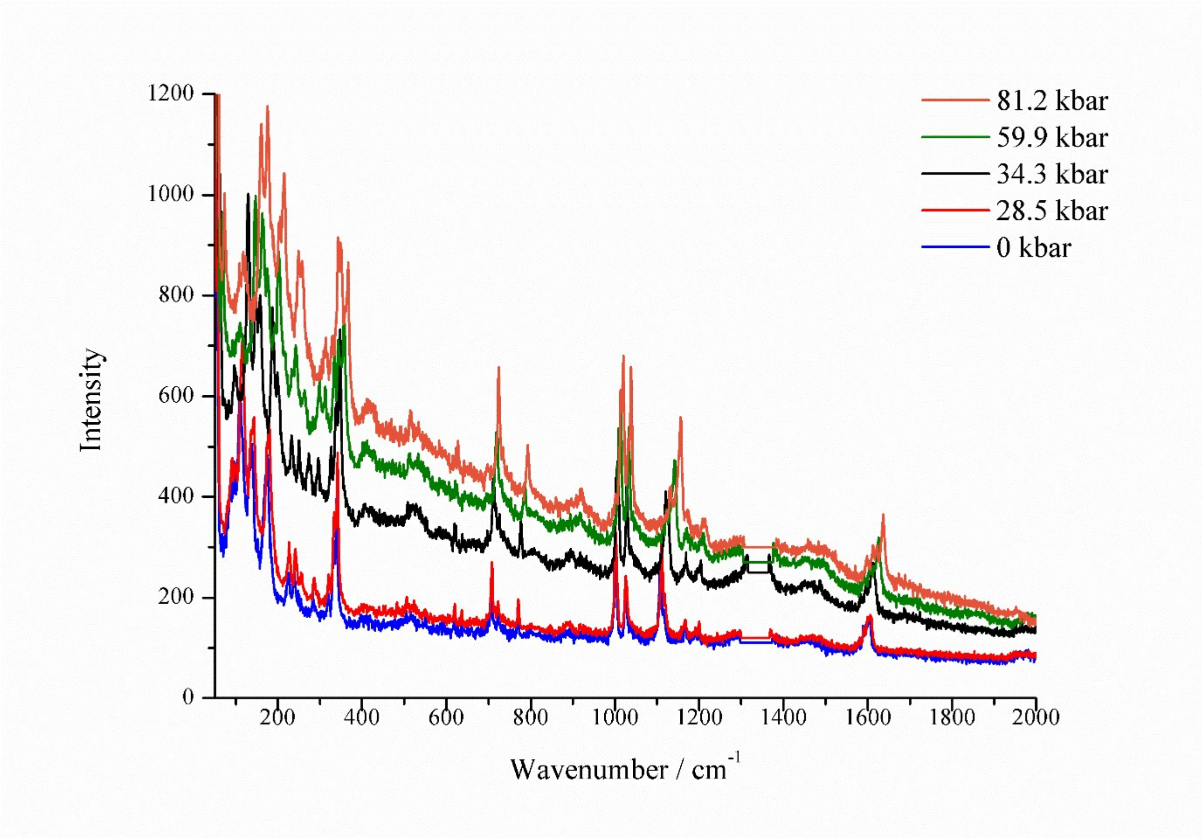

Figure S17. Raman spectra of **1** at various pressures.

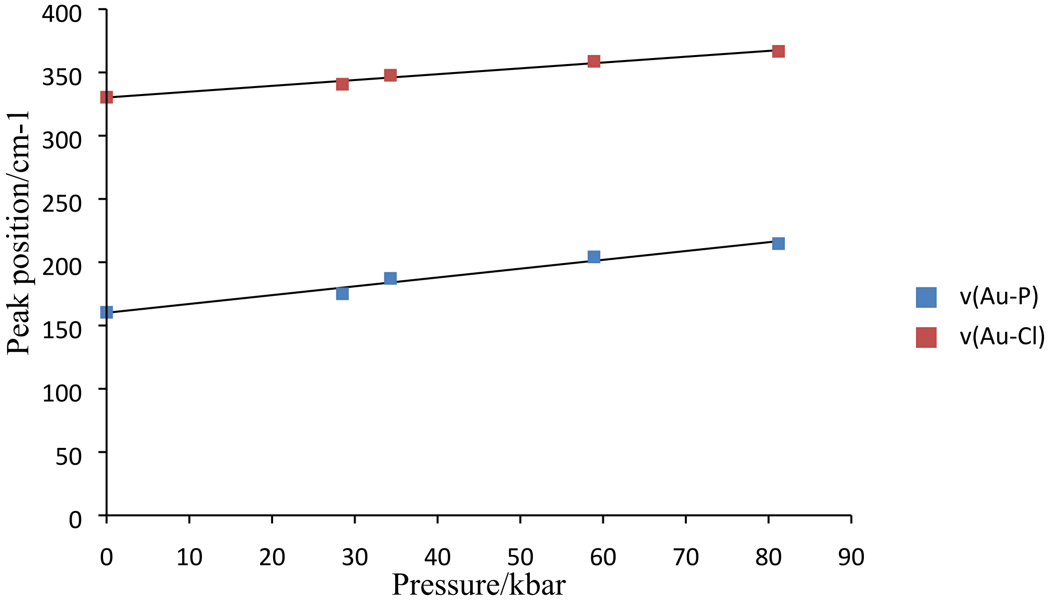

Figure S18. Variation in the peak position for *v*(Au−P) and *v*(Au−Cl) with increasing pressure.

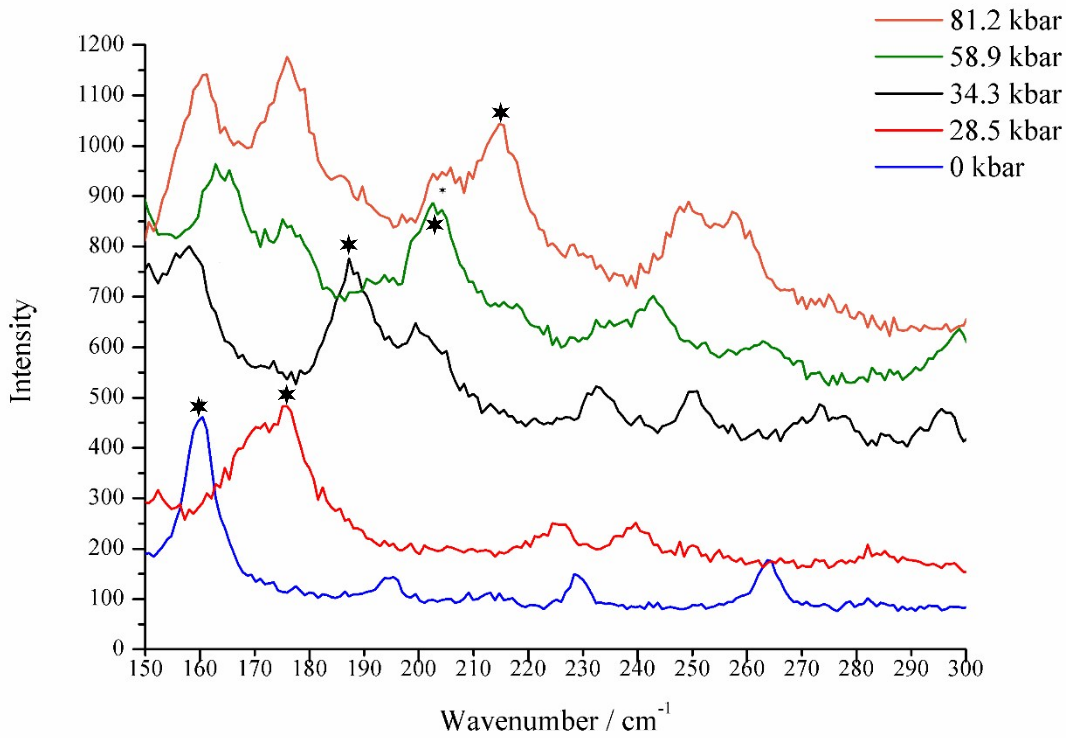

Figure S19. Variation in the *v*(Au−P) stretching frequency (identified by an asterisk) with increasing pressure.

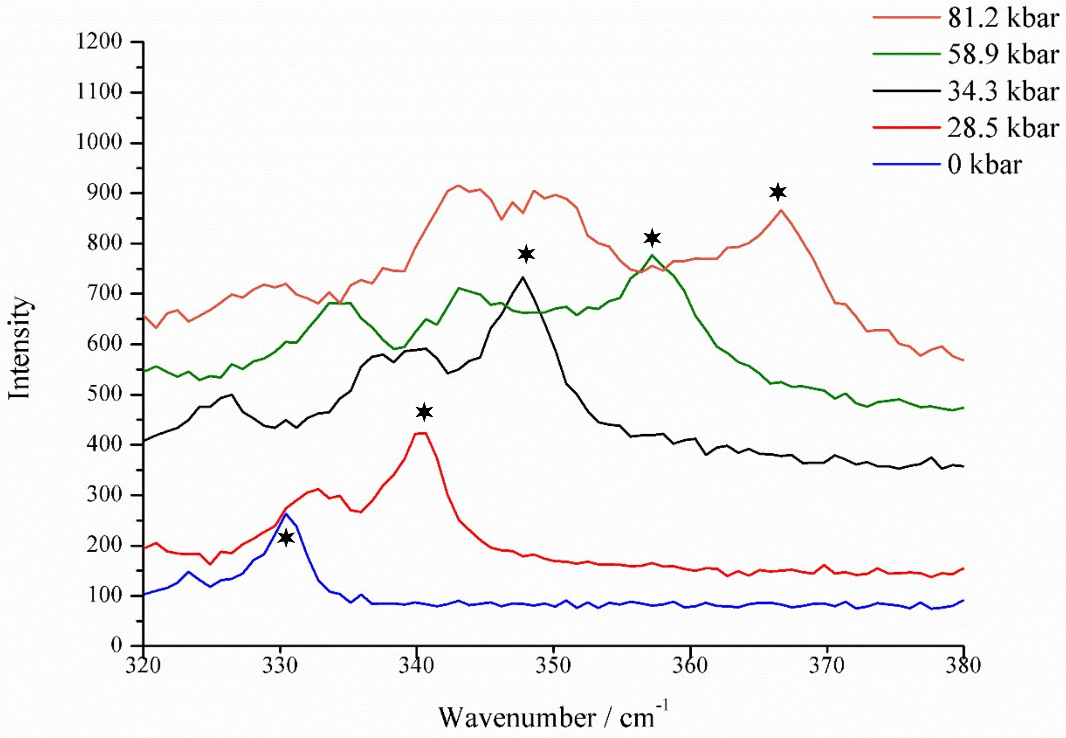

Figure S20. Variation in the *v*(Au−Cl) stretching frequency (identified by an asterisk) with increasing pressure.

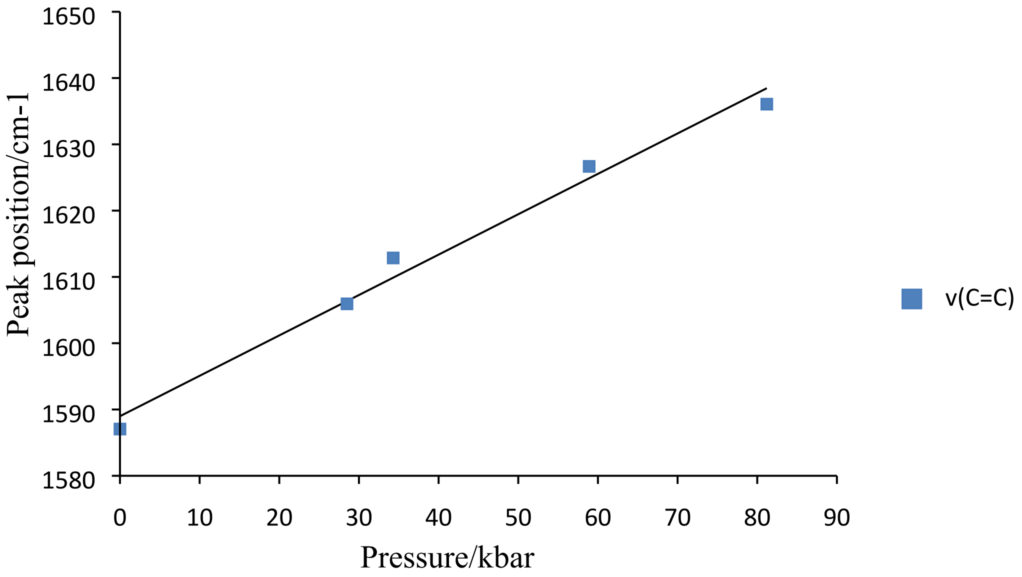

Figure S21. Variation in the peak position for *v*(C=C) with increasing pressure.

8. Conclusions

We have shown that high pressure crystallography offers a means to manipulate and modify the aurophilic interactions in Au(I) complexes, beyond what is feasible by chemical substitution. We can thereby investigate the Au···Au interaction in a controlled manner. We have also confirmed that the application of pressure can have major effects on these aurophilic interactions over the pressure range studied. The Au···Au distance in 1 decreases by 0.6132(13) Å, achieving the largest pressure-induced contraction in an Au···Au distance known to date. There is concomitantly a significant increase (> 50 cm^{-1}) in $v(Au_2)$ vibration energy. The decreasing response of the Au···Au interaction towards pressure can be attributed to the effects of the other intermolecular interactions present, which increase in number as a function of pressure. Detailed Hirshfeld surface analysis has revealed that the presence of intermolecular interactions other than the short π···π interactions are responsible for the formation of shorter Au···Au interactions. The results of theoretical calculations correspond well with the crystallographically-derived parameters and the Hirshfeld surface analysis and reveal that the repulsive interactions prevail over the attractive interactions, thereby preventing further shortening of intermolecular interactions in general, and the Au···Au separation in particular. High pressure Raman spectroscopy has provided additional insights into the effects of pressure on the complex. A combination of structural control *via* high pressure crystallography and structural design by chemical modification offers a potential future route to greater compression of the Au···Au distance, allowing the controlled formation of Au-Au bonds that can be characterised both structurally and spectroscopically.

9. References

1 J. Cámara, O. Crespo, M. Concepión Gimeno, I. O. Koshevoy, A. Laguna, I. Ospino, E. S. Smirnova, S. P. Tunik, *Dalton Trans*., 2012, **41**, 13891.

2 Oxford Diffraction (2008-2015). *CrysAlisPRO*. Oxford Diffraction Ltd, Yarnton, Oxford, England, UK.

3 Bruker 2001, *SADABS* (Version 2008/1). Bruker AXS Inc., Madison, Wisconsin, USA.

4 R. A. Forman, G. J. Piermarini, J. D. Barnett, S. Block, *Science*, 1972, **176**, 284.

5 G. M. Sheldrick, *Acta Crystallogr*., *Sect. C*, 2015, **71**, 3.

6 R. Angel, M. Alvaro, J. Gonzalez-Platas, *Zeitschrift für Kristallographie*, 2014, **229**, 405.

7 H. L. S. Wong, D. R. Allan, N. R. Champness, J. McMaster, M. Schröder, A. J. Blake, *Angew. Chem. Int. Ed*., 2013, **52**, 5093.

8 ADF2014, SCM, Theoretical Chemistry, Vrije University, Amsterdam, The Netherlands.

9 J. P. Perdew, K. Burke, M. Erzenhof, *Phys. Rev. Lett*. 1996, **77**, 3865.

10 Y. Akahama, H. Kawamura, *J. Phys*.: *Conf. Ser*., 2010, **215**, 1.